Presence and spatial distribution of interfacial electronic states in $LaMnO_3$-$SrMnO_3$ superlattices

A. B. Shah,[1,2] Q. M. Ramasse,[3] S. J. May,[4] Jerald Kavich,[4] J. G. Wen,[2] X. Zhai,[2,5] J. N. Eckstein,[2,5] J. Freeland,[6] A. Bhattacharya,[4,7] and J. M. Zuo[1,2]

[1]*Department of Materials Science and Engineering, University of Illinois at Urbana–Champaign, Urbana, Illinois 61801, USA*
[2]*Fredrick Seitz Materials Research Laboratory, University of Illinois at Urbana–Champaign, Urbana, Illinois 61801, USA*
[3]*National Center for Electron Microscopy, Lawrence-Berkeley National Laboratory, Berkeley, California 94720, USA*
[4]*Materials Science Division, Argonne National Laboratory, Argonne, Illinois 60439, USA*
[5]*Department of Physics, University of Illinois at Urbana–Champaign, Urbana, Illinois 61801, USA*
[6]*Advanced Photon Source, Argonne National Laboratory, Argonne, Illinois 60439, USA*
[7]*Center for Nanoscale Materials, Argonne National Laboratory, Argonne, Illinois 60439, USA*

(Received 6 February 2010; revised manuscript received 22 July 2010; published 13 September 2010)

We report direct evidence of interfacial states at the onset of O *K* edge confined to a spatial distance of 1 unit-cell full-width at half maximum at the sharp interfaces between epitaxial films of $LaMnO_3$ and $SrMnO_3$ from electron energy-loss spectroscopy (EELS) measurements. The interfacial states are sensitive to interface sharpness; at rough interfaces with interfacial steps of 1–2 unit cells in height, experimental data shows a reduction, or suppression, of the interfacial states. The EELS measurements were performed using a fine electron probe obtained by electron lens aberration correction. By scanning the electron probe across the interface, we are able to map the spatial distribution of the interfacial states across interfaces at high resolution.

DOI: 10.1103/PhysRevB.82.115112 PACS number(s): 79.20.Uv, 73.21.Cd, 68.65.Cd

I. INTRODUCTION

The ability to nucleate new electronic states at coherent interfaces between two oxides has generated considerable excitement recently.[1–6] Correlated-electron interfaces, such as the surface and interface of crystals, have a tendency to reconstruct.[3,7] Interfacial electronic reconstruction was first suggested between the Mott and band insulators of $LaTiO_3$ (LTO) and $SrTiO_3$ (STO), which is metallic.[1] The interface between $LaMnO_3$ (LMO) and $SrMnO_3$ (SMO) is another system that has shown unique electronic and magnetic properties that are attributed to interface electronic reconstruction.[6,7] In bulk form, LMO is a Mott insulator with a $t_{2g}^3 e_g^1$ configuration while SMO is a band insulator with a $t_{2g}^3 e_g^0$ electronic configuration. In the series of $(LMO)_{2n}/(SMO)_n$ superlattices, experiments have shown that the proximity to the interfaces between LMO and SMO induces a metal-insulator transition highly dependent on n; the system is metallic for $n \leq 2$ and insulating for $n \geq 3$.[4,5] In both STO/LTO and LMO/SMO interfaces, charge leakage on the scale of a few unit cells (u.c.) has been suggested as the cause of interfacial electronic reconstruction.[3,7,8] In the case of the LMO/SMO interface, linear and circular magnetic dichroism in the Mn $L_{2,3}$ x-ray absorption spectra demonstrate in-plane interfacial ferromagnetic order attributed to the charge redistribution across interfaces.[9] Charge-density calculations indicated that the e_g level in SMO is not occupied except in a narrow region near the interface.[9] Resonant soft x-ray scattering (RSXS) (Ref. 10) of a LMO/SMO superlattice revealed extra states above the Fermi level, which was attributed to the quasiparticlelike states formed at the interface of Mott and band insulators. Nakao *et al.* detected a difference in Manganese (Mn) scattering at the LMO/SMO interface by studying the energy dependence of scattering intensity near Mn *K* edge.[11] However, these measurements do not provide direct information about the location and spatial distribution of the interfacial states.

To look for evidence of interfacial electronic reconstruction and study its spatial distribution at selected interfaces, we have carried out a combined structural and spectroscopic study of a $(LMO)_{11.8}/(SMO)_{4.4}$ superlattice using aberration corrected scanning transmission electron microscope (STEM) imaging, electron energy-loss spectroscopy (EELS) and electron nanodiffraction. The same superlattice was previously studied by polarized neutron reflectivity (PNR), which revealed an enhanced, spatially confined (~3 u.c.), ferromagnetic moment at the LMO/SMO interfaces.[12] However, in the same superlattice the ferromagnetic moment is suppressed at the SMO/LMO interfaces, which had a wavy, stepped structure compared to the smooth, sharp, LMO/SMO interfaces. One of motivations of this study is, thus, to map the possible difference in the electronic structure at the two different LMO and SMO interfaces. The benefits of aberration correction are the small and intense beam, which probes the interface with increased resolution and greater signal to noise ratio than the previous generation of STEMs.[13–16] Using this, we probed the electronic structure across the $(LMO)_{11.8}/(SMO)_{4.4}$ superlattice by examining the fine structure of Oxygen (O) *K*, Mn $L_{2,3}$, and Lanthanum (La) $M_{4,5}$ edges. The EELS study was performed in combination with structural characterization using high-angle annular dark field (HAADF) STEM (known as Z contrast) imaging and electron diffraction. We show that the interfacial states expected from interfacial electronic reconstruction are present at the sharp interface. The interfacial states are suppressed at rough interfaces of LMO and SMO. Furthermore, from EELS mapping, we are able to determine the spatial extent of the interfacial states to ~1 u.c. at the sharp interface.

II. EXPERIMENT

The LMO and SMO superlattice was grown on a (001) STO substrate (a=3.905 Å) layer by layer at 700 °C by

ozone assisted molecular-beam epitaxy.[17] Details about the growth can be found in Ref. 10. The x-ray reflectivity data yielded a composition of $(LMO)_{11.8}/(SMO)_{4.4}$ for the superlattice.[12] X-ray absorption spectroscopy (XAS) was acquired from a piece of the same sample at beamline 4-ID-C of the Advanced Photon Source. The circularly polarized x-rays were incident at an angle of approximately 45° from the sample surface. Data was acquired simultaneously in the total electron yield (EY) (few nanometer probing depth) and total fluorescence yield (FY) (~50–100 nm probing depth). For the Mn *L* edge, we present the EY data which probes the top LMO/SMO bilayer. Data in the FY mode shows a similar result but with poorer signal to noise due to the low fluorescence yield at these energies. For reference, a sample of a $SrMnO_3$ film was also grown on $SrTiO_3$ under the same conditions as the superlattice.

The specimen for electron microscopy was prepared by wedge polishing at a 1° angle and ion milled in a Gatan model 691 Precision Ion Polishing System for several hours at 4.0 kV and fine polished at 2.0 kV for 20 min. The specimen was plasma cleaned and transferred directly to the microscope for observation. A JEOL JEM 2010F operated at 197 kV was used to obtain electron nanodiffraction patterns. High spatial resolution EELS in STEM mode was performed on the TEAM 0.5 microscope, which is equipped with a model 865 Gatan Image Filter Tridiem ER for EELS.[18] The microscope was operated at 80 kV to reduce knock-on damage to the sample. After tuning the aberration corrector, the spherical aberration coefficient (Cs) is $\sim\pm 5$ um and the chromatic aberration coefficient (C_c) is ~2.1 mm. The probe size used for STEM-EELS is 1.5 Å and the energy resolution for EELS collected with the monochromator set to unfiltered mode is 0.8 eV measured by the full-width at half-maximum (FWHM) of the zero-loss peak. The spectrum acquisition was set at 0.1 eV/channel dispersion. The O *K* and Mn $L_{2,3}$ EELS spectra were background subtracted with a power law fitted using a simplex optimization routine. There is a small variation in the dispersion of the recorded spectra; the O *K* edge has a dispersion of 0.1 eV/channel while the Mn *L* edge dispersion is slightly smaller. The Mn *L* edge dispersion was calibrated with XAS spectra recorded at 50 K and EELS spectra acquired in a JEOL JEM2010F microscope operated at 197 kV. La $M_{4,5}$ EELS spectra were acquired in separate line scans from the O *K* and Mn *L* edges, and are background subtracted with a power law implemented in the GATAN DIGITAL MICROGRAPH software package. High spatial resolution HAADF STEM imaging was performed on a JEOL JEM2200FS operated at 200 kV with a CEOS third-order spherical aberration corrected probe [$C_s \approx \pm 5$ um, $C_c \approx 1.4$ mm (Ref. 19)]. At the optimum imaging conditions, the STEM HAADF resolution is 1 Å.[20]

III. ATOMIC STRUCTURE OF THE SUPERLATTICE

The atomic structure of the superlattice is a combination of the atomic structure of the constituent La-Mn-O and Sr-Mn-O layers, their interfaces and the interface with the $SrTiO_3$ substrate. The $SrTiO_3$ substrate has a cubic perovskite crystal structure of the $Pm\bar{3}m$ symmetry with a lattice parameter of $a=3.9051$ Å. In bulk form, $LaMnO_3$ at room temperature has an orthorhombic structure of the *Pbmn* symmetry with lattice parameters of $a=5.5367$ Å, $c=5.7473$ Å, and $b=7.6929$ Å.[21] The stochiometric $SrMnO_3$ has a hexagonal structure with lattice parameters of $a=5.449$ Å and $c=9.078$ Å. Negas and Roth reported that a perovskitelike, oxygen deficient, phase of $SrMnO_{3-x}$ (with $x\sim 0.3$) can be stabilized at room temperature by quenching from a high temperature of about 1400 °C.[22] This anion deficient perovskite phase can be reoxidized at low temperatures to give a nearly stochiometric cubic $SrMnO_3$ with $a=3.806$ Å.

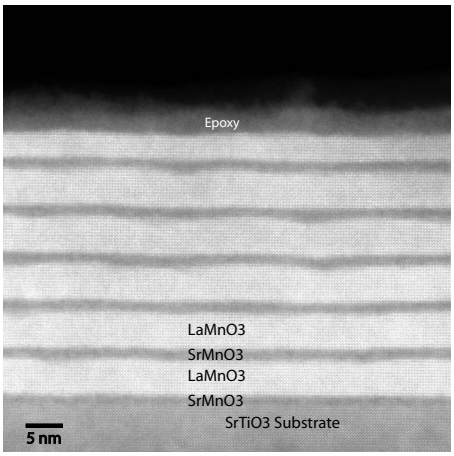

FIG. 1. STEM image of the superlattice acquired at 80 kV. The dark films are $SrMnO_3$ and the lighter films are $LaMnO_3$. Each $LaMnO_3$ film contains valleys that are filled by $SrMnO_3$. The valleys propagate in the $LaMnO_3$ film as growth proceeds.

Figure 1 shows an annular dark field STEM image of the superlattice in cross section at a medium-high magnification acquired at 80 kV. The SMO layers appear as the darker thin films and the LMO layers are the brighter thicker films. In this image, atomic columns of Sr, Mn, and La are resolved while O columns are not observed due to weak scattering of light atomic columns. The image shows a coherent lattice between the films and the substrate. A survey of the films over a larger area revealed no misfit dislocations. In all films, the top (away from the substrate) LMO-SMO interface is sharp to a single unit cell and the bottom (toward the substrate) SMO-LMO interface is rough to 2–3 u.c. The SMO-LMO interface can be described as a series of flat regions and valleys. A thin film of SMO was first grown on the STO substrate. The first LMO film has a sharp interface with the underlying SMO film. The roughness at the next SMO and LMO interface appears to have developed during growth from surface roughening on the growth front of the LMO film. The overlying SMO film fills the valleys and the next LMO film grows sharp on top of Sr-Mn-O and this process repeats itself. The propagation of the valley through the superlattice occurs approximately at a 30° angle to the growth direction. Throughout the specimen, the valleys were found repeating every 10–20 nm horizontally. At a field of view of 50×50 nm, typically two valleys are seen in each supercell along the width of the image. The last LMO film is grown thinner than the underlying films. The surface of this last film

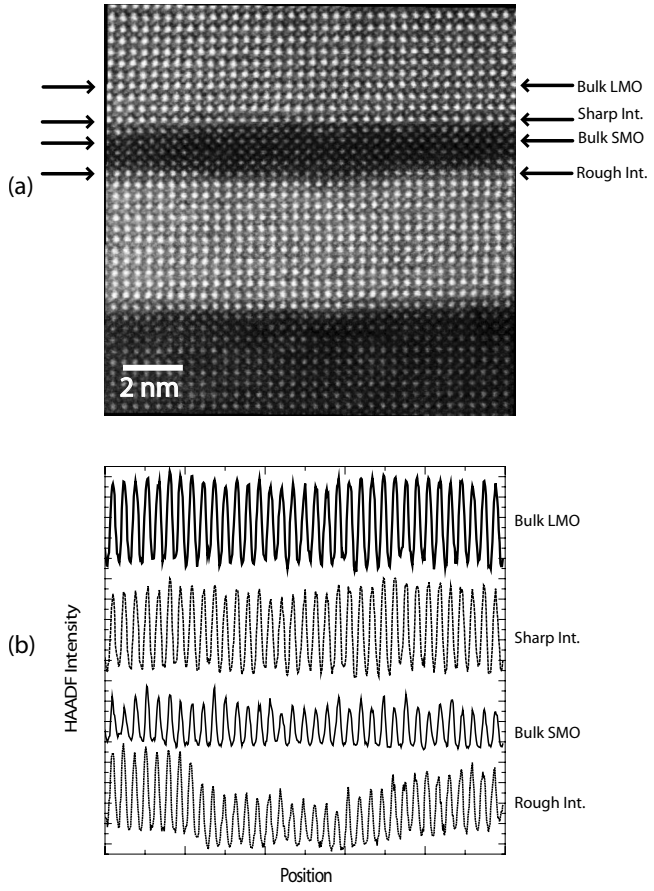

FIG. 2. (a) High magnification STEM image acquired at 200 kV with line profile markers. (b) Line profile through the films and interfaces. Note that the line profiles go through nearly the entire horizontal of the image. The upper $LaMnO_3$-$SrMnO_3$ interface is sharp while the lower $SrMnO_3$-$LaMnO_3$ interface is rough to 1–2 u.c. The line profiles are vertically shifted for clarity.

was protected by an epoxy during sample preparation. The contrast from the STEM image clearly shows the roughness of this final film.

To characterize the interfacial roughness, we imaged the superlattice at high magnification using atomic resolution HAADF-STEM at 200 kV. The contrast difference between La and Sr from the Z-dependence provides a good indication of the interfacial roughness. Figure 2 shows an example of a high magnification STEM image. We took horizontal line profiles parallel to the substrate through the La and Sr atomic columns. The intensity in the middle of the LMO film is high, due to the scattering from the high-Z La columns. The intensity through the middle of the SMO film is lower. The intensity is fairly uniform with the average peak intensity of the Sr atomic columns at the level of about 40% of the average peak intensity of the La atomic columns. The intensity at the sharp LMO-SMO interface is about the same as the LMO and uniform whereas the intensity at the rough SMO-LMO interface varies from the low Sr signal to the strong La signal. The HAADF signal shows the columns in the middle of this line profile are La deficient. SMO fills in the LMO valleys and recovers sharp films. Evidence of film sharpness from the La EELS profile is presented in the next section.

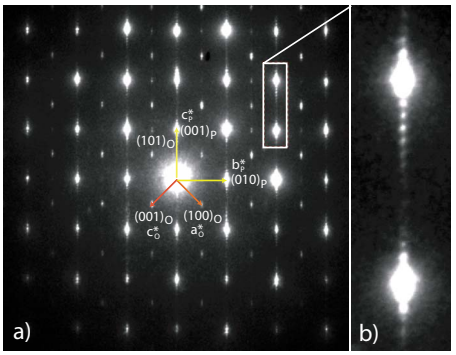

FIG. 3. (Color online) (a) Nanoarea electron-diffraction pattern of the superlattice shows satellite peaks corresponding to a periodic structure. The films in the superlattice are coherently strained to the STO substrate. A survey of high-resolution STEM images in the sample revealed no defects near the substrate-superlattice interface. The weak reflections correspond to orthorhombic $LaMnO_3$. (b) Magnified view of the superlattice reflections shows a high quality, periodic structure.

Figure 3 shows a diffraction pattern recorded from the superlattice using a electron nanoprobe of 80 nm in diameter placed on top of the superlattice and the vacuum. The probe has a divergence angle less than 0.05 mrad.[23] A diffraction pattern was also recorded from the STO substrate near the superlattice (not shown) and used for calibration. The diffraction pattern consists of diffraction spots from the average lattice and weak superlattice reflections in the vertical direction. The superlattice is fully coherent as evidenced by the matching of the substrate and superlattice diffraction spots in the in-plane, (010) direction. We used two different average lattices for indexing the diffraction pattern, the lattice of a simple perovskite, which is marked with P, and the lattice of orthorhombic $LaMnO_3$, which is marked with O. For the lattice of a simple perovskite, we assumed the incident beam is along the a^* axis and the c^* axis is perpendicular to the superlattice (out-of-plane). The sharp diffraction spots along the b^* axis (in-plane) shows that the superlattice and the substrate lattice are fully coherent. This agrees with our STEM imaging results, which show no misfit defects at the superlattice-substrate interface. Using the calibration of the STO substrate, we measured the average c-axis lattice parameter of the superlattice from Fig. 3. The result is $c_{SL}=3.873\pm0.001$ Å. Independent x-ray measurements of the same superlattice give a similar value of $c_{SL}=3.874\pm0.003$ Å. The c axis is considerably shorter than the b axis (3.9051 Å) parallel to the substrate. The diffraction spots indexed by the simple perovskite lattice are the strong reflections shown in Fig. 3. Between these strong diffraction spots, there are another set of weaker diffraction spots. The stronger ones among these weak reflections can be indexed based on the orthorhombic lattice of the $LaMnO_3$ with the electron beam along the b^* axis. The $(100)_O$ and $(001)_O$ marked in Fig. 3 are the two fundamental reflections for this orientation. A set of much weaker reflections belonging to the $[101]_O$ of the orthorhombic lattice can also be seen in the diffraction pattern. These results suggest an orthorhombic, distorted, perovskite structure for the relatively thick LMO films in the superlattice. This is consistent with

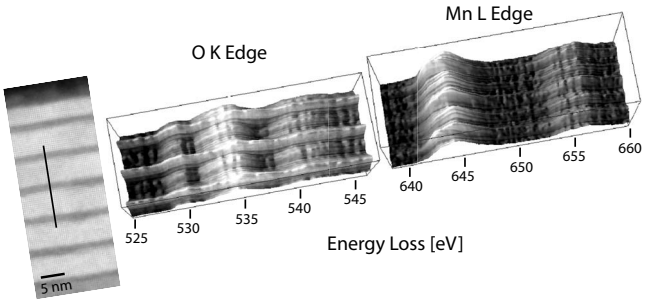

FIG. 4. As-recorded O *K* edge and Mn $L_{2,3}$ spectrum images from the line marked in the STEM image. The sampling is 1 point per 2 Å and the spectrum images are smoothed to display the major edge features. When the electron beams moves from LMO to SMO, the O *K* prepeak rises and the Mn L_3 peak maximum shifts toward lower energy loss.

the findings of Aruta *et al.*,[24] who concluded that LMO films of 10 u.c. or thicker in the superlattice prefer the same orbital ordering (distorted perovskite) as thick LMO films grown on STO.

The superlattice reflections between two diffraction spots of the average lattice from the box region of Fig. 3(a) are shown in Fig. 3(b). The sharp diffraction spots indicate a high-quality periodic structure. The distance between the superlattice reflections is measured at 0.00262 1/Å, corresponding to a real-space period of 16.5 times the average lattice. The period measured by diffraction is an average of all supercells under the electron probe (the full superlattice in this case). The noninteger supercell repeat period, thus, is a result of averaging over the imperfect superlattice structure as evidenced by Figs. 1 and 2. An examination of Fig. 1 shows some of the LMO-SMO layers have a supercell thickness 16 times the average lattice while others are 17 times. Additionally, the topmost supercell is only 13 layers thick. There is no evidence of missing Mn-O, or La-O, or Sr-O planes in high-resolution images such as Fig. 2.

IV. PROBING THE ELECTRONIC STRUCTURE OF THE SUPERLATTICE

We use EELS spectra recorded along lines perpendicular to the superlattice and the interfaces to characterize their electronic structures. Figure 4 shows an example of EELS line-scan spectra and corresponding STEM image. The spectra shown in the three-dimensional surface plot correspond to an unprocessed line scan with the energy detection window of the EELS spectra centered around the O *K* edge and Mn $L_{2,3}$ edge. The surface plot is smoothed to show the major changes in the shape of electron-energy core losses among different layers. The EELS spectra were acquired in 2 Å steps. As the probe moves from a LMO layer to a SMO layer, the O *K* prepeak rises while the second peak shifts toward higher energy loss. The spectra were recorded in a region of relatively uniform sample thickness of ~0.5 mean-free paths in the four supercells closest to the substrate (The average estimated mean-free paths of LMO and SMO is 75 nm at 80 kV). To study the interfacial electronic structure, we analyzed the core loss EELS fine structure. The results of these studies are described below.

The Mn $L_{2,3}$ edge represent transitions from $2p_{1/2}$ to $2p_{3/2}$ states to the unfilled 3*d* states. Their use for the study of Mn valences are well documented.[25–27] Fig. 5(b) displays the background subtracted Mn $L_{2,3}$ edges recorded along the downward linescan as indicated in Fig. 5(a). The spectra were normalized following the edge from 675 to 695 eV. There are a total of 80 spectra in Fig. 5(b) with a real-space sampling of 2 Å between spectrum integration points; they are labeled from spectrum number 0 to number 79. The L_3 edge in Fig. 5(b) shows the most change in fine structure while the change in the L_2 peak, which is weaker, is less obvious. The change in the L_3 edge fine structure appears as a shift of the L_3 peak maximum position, which gives the wavy appearance of the L_3 edge map as the electron probe scans across the superlattice. The change in the L_3 fine structure is further examined in Fig. 5(c), which plots the L_3 edge for spectra number 5 to 20 across the first SMO layer. The spectra number 9–14 are similar with the peak maximum shifted by ~1.2 eV toward lower energy loss; these spectra were recorded with the electron probe inside SMO. However, there is no obvious shift in the onset of the L_3 edge, which would have indicated a valence change. A strong shift of the L_3 onset and peak positions was measured by Kurata and Colliex in an EELS study of bulk manganese oxides where Mn ions are known to have several valences.[25] However, the strong shift of the L_3 maximum was not observed in previous work on similar $LaMnO_3$-$SrMnO_3$ superlattice samples.[28,29] Rather a small shape change in the L_3 peak was observed. Verbeeck *et al.*[28,30] proposed if the Mn concentration was constant in their LMO-SMO superlattice, the lack of a chemical shift has been suggested to result from either oxygen vacancies in the SMO film or the covalent Mn-O bond rather than a purely ionic bond. We also note that the shift of the L_3 maximum is more abrupt at the sharp interface and gradual at the rough interface. This is clear at the interfaces of the first and third SMO films in the spectrum image of Fig. 5. In the second SMO film, the shift is smaller, due to varying interface roughness at the interfaces of the three SMO films. In Fig. 5(c), the sharp interface is characterized by the abrupt transition from spectrum number 8 to number 9 while the rough interface is characterized by an additional interfacial spectrum, number 15, which is quite different from the spectrum number 14 from SMO and number 16 (16 is more characteristic of LMO). At the sharp interface, the Mn spectrum is unique from the spectra in the middle of the LMO and SMO film. At the rough interface, the Mn spectrum is similar to an average of LMO and SMO spectra. The presence of an abrupt shift in the maximum of the Mn *L* edge at the sharp LMO-SMO interface indicates that any change in the Mn electronic states from interfacial electronic reconstruction is likely confined to 1 u.c.

The interface sharpness is further characterized by EELS line scans of the La $M_{4,5}$ edge. Figure 5(d) shows a STEM image and Fig. 5(e) show the integrated intensity of the La $M_{4,5}$ edge through the line profile at 60° to the interface. The EELS spectra were acquired in ~2.5 Å steps and the integrated intensity in integrated from 832 to 854 eV. The integrated intensity shows the interfaces are asymmetric with

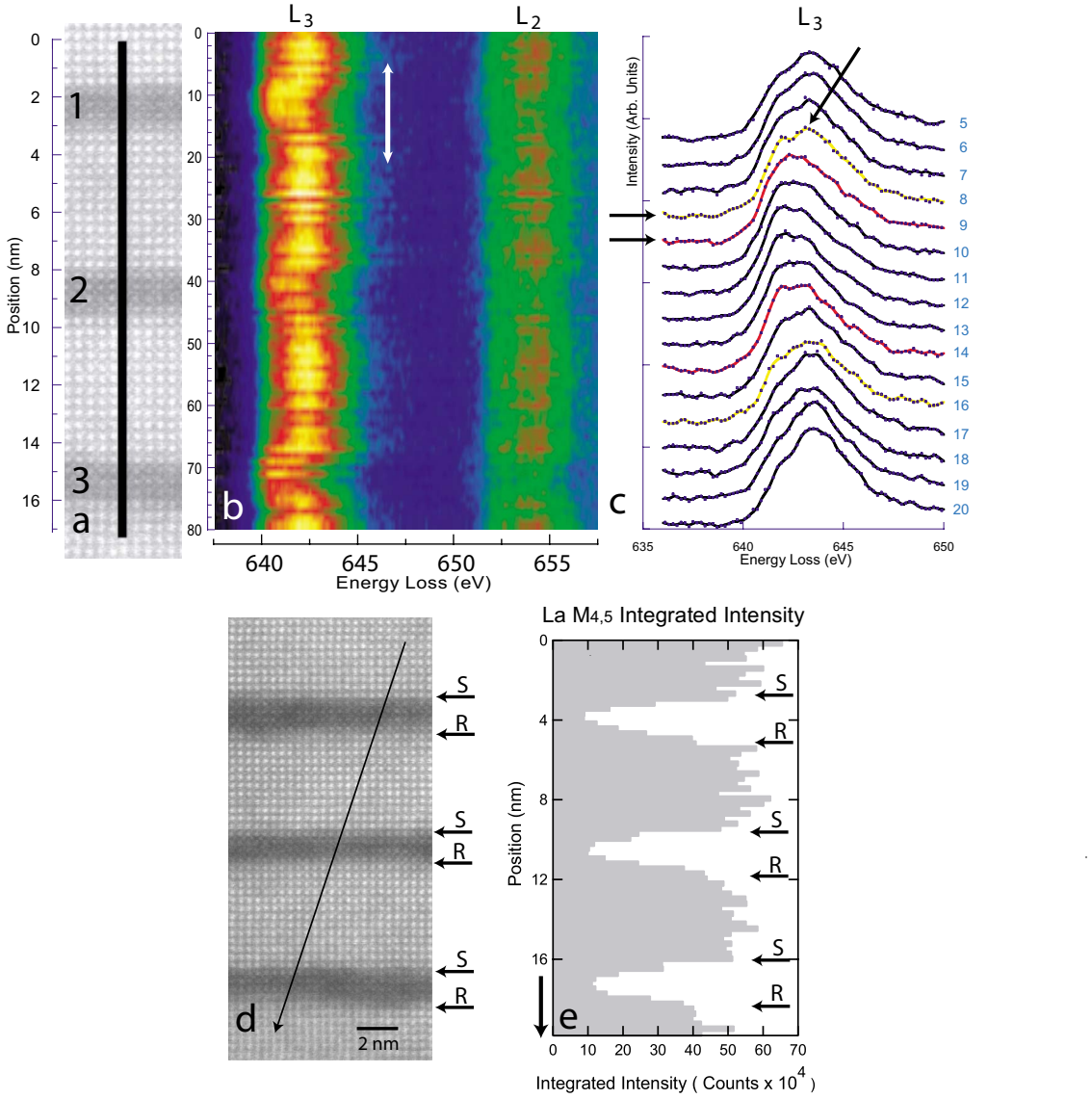

FIG. 5. (Color online) (a) HAADF STEM image showing the line where EELS spectra were recorded. (b) EELS spectrum image acquired in 2 Å increments. There is a small periodic modulation in EELS intensity as the electron probe moves on and off Mn columns. The Mn L_3 edge maximum shifts toward lower energy loss in the $SrMnO_3$ film. (c) Individual Mn L_3 spectra through the LMO-SMO and SMO-LMO interfaces from the part of (b) marked by the double white arrows. At the sharp interface, there is an abrupt change in the disappearance of the peak marked by arrow from spectrum 8 to 9. Near the rough interface, there is a smoother shift toward lower energy loss. (d) STEM image where a La EELS profile was acquired. (e) The integrated intensity of the La M edge from 832 to 854 eV shows the La/Sr intermixing is primarily limited to 2–3 u.c. at the bottom rough interface. The upper interface is sharp to a single unit cell.

regard to La/Sr intermixing. The LMO/SMO interface is sharp to a single unit cell while the SMO/LMO interface is rougher to 2 to 3 u.c. The remaining La signal in the SMO films is from the large EELS delocalization tails for the La $M_{4,5}$ edge.

Figure 6 shows the Mn $L_{2,3}$ edge averaged from five EELS spectra in the LMO and SMO films. The figure also shows the sum of all EELS spectra in the line scan of Fig. 5 (80 spectra). The L_3 edge of the LMO film is peaked at 642.5 eV. A small shoulder is visible at ~641 eV. This was also seen in the XAS of bulk LMO at ~640.5 eV,[31] which was attributed to multiplets by the spin-orbit splitting of the Mn $2p$ core hole. In the SMO films, the Mn L_3 edge peak is characterized by a relatively flat top, which is shifted to lower energy loss with respect to the Mn L_3 edge of LMO. An XAS spectrum of a reference SMO film grown on STO shows several shoulder peaks and a primary peak at ~643 eV. The EELS spectrum from the middle of the SMO film in the superlattice, in comparison, is narrower and the contribution from the primary peak is relatively weak. Both films of LMO and SMO have spectra of Mn L_3 edge different from the bulk references; this observation is consistent with the findings of previous EELS studies.[28–30] A summation of all of the 80 EELS spectra in the linescan of Fig. 6 matches well with XAS data of the superlattice, which shows the same shoulder on the L_3 edge. The two methods reveal

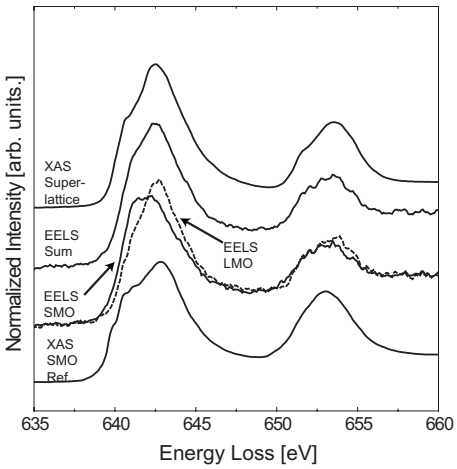

FIG. 6. A comparison of Mn $L_{2,3}$ edge in XAS and the summed intensity of all spectra in the EELS linescan marked in Fig. 5 shows good agreement between the spectra other than differences in energy resolution of the techniques. The spectra also verify electron-beam damage was avoided as the fine structure and ratios of L_3 to L_2 edges are the same. The averaged spectrum from the center of the LMO film does not have a shoulder on the L_3 edge that bulk LMO samples showed in Ref. 31 Likewise, the averaged spectrum from the center of the SMO film does not have two local minimum on the L_3 edge that a bulk SMO film grown on STO shows. The electronic configuration of both LMO and SMO films in the superlattice differs electronically from bulk samples.

that the Mn cation has a different electronic configuration in the two films; the Mn configuration in SMO is unique from bulk references without a strong splitting of the shoulder and a dominant the L_3 peak. Rather the shoulder and main peak are of roughly equal intensity and merge as one broader peak. Additionally, the ratio of the Mn L_3/L_2 edge changes little, if at all, anywhere in the superlattice, including the interfaces. This can be seen in Fig. 6, where the Mn $L_{2,3}$ edge of LMO is plotted on top of the SMO as the dashed line.

Figure 7 shows the O K core loss edge obtained by averaging spectra from the center of each of the oxide films and the spectrum averaged for the three sharp and rough interfaces as observed in Fig. 5. The spectra are background subtracted with a power law and normalized following the edge from 550 to 610 eV. The continuous lines are smoothed fits to the experimental data. The O K core loss edge contains several peaks which represent O 1s transitions to O 2p states hybridized with metal states.[30,31] The first peak, which we refer to as the prepeak centered at ~530 eV, is attributed to O 2p unoccupied states hybridized with Mn 3d states. The second peak centered at ~535 eV is from O 2p unoccupied states hybridized with La 5d or Sr 4d. The prepeak is sensitive to changes in oxidation state as seen in bulk Mn oxides[25,32,33] and perovskite multilayer films.[29,30,34,35] As the probe moves from LMO to SMO, the prepeak intensity rises by ~20%. The second peak develops additional features; overall, the peak broadens and shifts toward higher energy loss. The maximum intensity of second peak is about twice as intense as the prepeak. This behavior was also observed by Verbeeck *et al.*[30] on $LaMnO_3$-$SrMnO_3$ superlattices. However, in both Verbeeck's work and the results shown here, the height of the prepeak does not rise to the level as measured by XAS studies of bulk alloys of LMO and SMO,[31] where the prepeak rises greater than second peak as the doping of Sr onto La sites in $LaMnO_3$ exceeds 60%. The fine structure of the O K edge does not match bulk manganese oxides compounds with 4+ and 3+ Mn ions from Refs. 25, 26, and 36 where the prepeak is much stronger such that the second peak is masked. The EELS shows that the super-

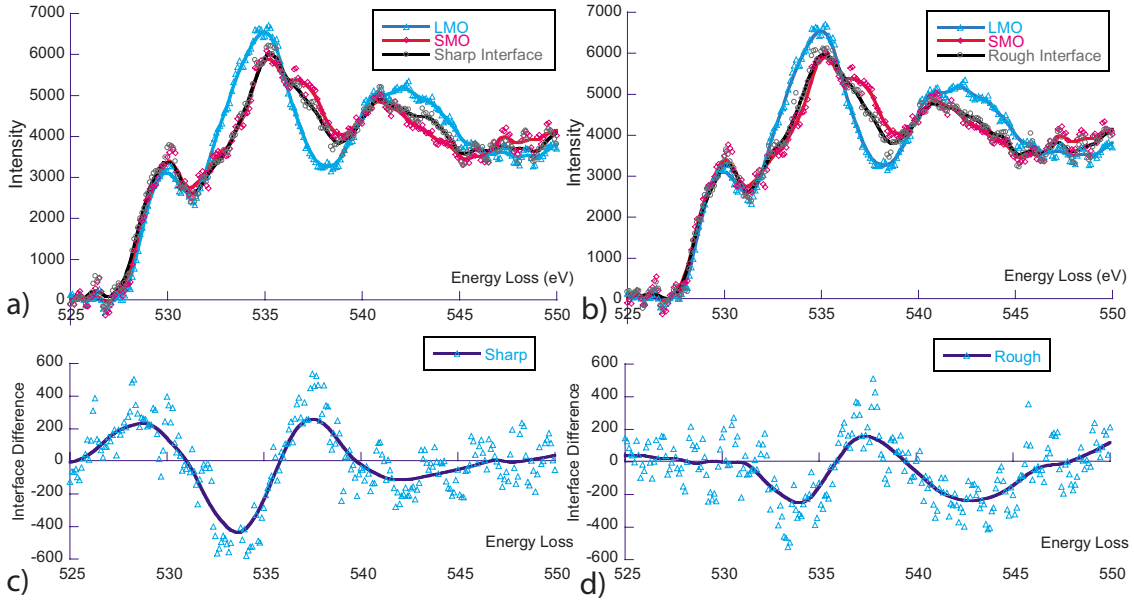

FIG. 7. (Color online) O K edge spectra from an average of the center spectrum of the LMO film, SMO film, (a) sharp interface and (b) rough interface. The prepeak shows the hybridization with Mn 3d states is unique in each case. (c) An average of the LMO and SMO spectrum is subtracted from the sharp interface spectrum, showing the difference. There are extra states at the onset of the edge, which are above the Fermi-energy level. (d) The same difference method is applied to the rough interface spectrum, where there are no extra states at the onset. The O K edge spectrum at the sharp interface is a unique electronic configuration.

lattice thin films have fewer unoccupied hybridized O $2p$ states than the bulk oxide materials with the same expected valence.

The interfacial O K spectra are different from the average spectrum from the center of SMO and LMO films; they are also different from each other. To compare these spectra; we first calculated the difference spectrum according to

$$\Delta I(z,\Delta E) = I^{Interface}(z,\Delta E) - [I^{\mathrm{LMO}}(z,\Delta E) + I^{\mathrm{SMO}}(z,\Delta E)]/2. \quad (1)$$

The results are then averaged for the sharp and rough interfaces and plotted in Fig. 7. The fit of the difference spectrum from the sharp interface clearly reveals additional spectral weight near the onset of the O K prepeak, from 526 to 531 eV. This additional spectral weight is peaked at 528.5 eV. The difference spectrum obtained for the rough interface are flat near zero near the onset of the O K prepeak. The difference between the sharp and rough interfaces are consistent with the PNR result, which revealed an enhanced ferromagnetic moment at the sharp LMO/SMO interfaces and reduced ferromagnetic moment at the rough interface.[4,12]

The second peak of the interfacial O K edge follows SMO on the lower energy-loss side and is in between SMO and LMO on the high energy-loss side. This peak has been attributed to hybridizations of O $2p$ states with Sr $4d$ in case of SMO or La $5d$ states in LMO. In bulk $La_{1-x}Sr_xMnO_3$, this second peak changes shape and shifts toward higher energies when x increases from 0 to 0.9 corresponding to increasing replacement of La^{3+} with Sr^{2+}.[31] These effects are explained by to the gradual crossover from bands of La $5d$ to bands of Sr $4d$ character in the random alloy of $La_{1-x}Sr_xMnO_3$. Compared to this, especially the XAS spectrum at the composition $x=0.5$ that is expected at the interface, the features of the second peak for the interfacial O K edge is quite different;[31] the similarity with SMO on the lower energy side of the second peak suggests a strong Sr character at the interface.

To examine the spatial distribution of the interfacial states, we extended the difference spectrum analysis to all O K EELS spectra of Fig. 4 to obtain a difference map. The as-obtained difference map contains significant noise due to gain variations in pixels of the CCD detector. To reduce the noise, we combined 8 pixels along the energy-loss direction in the difference map into a single pixel, which reduced the energy dispersion from the original 0.1 eV/channel to 0.8 eV/channel. The reduced map was then smoothed using a 3×3 Gaussian filter in the energy loss and spatial directions. The results are plotted in Fig. 8(b) together with the HAADF-STEM image and the map of the Mn L_3 edge. Four spectral peaks (weights) are identified and labeled as 1–4 in the difference map in the energy range between 526.7 and 530.3 eV as indicated by arrows. The center of these peaks in the spatial direction coincides with the LMO-SMO interfaces as indicated by the white lines and their positions in the background subtracted Mn L_3 edge map. Figure 8(d) examines the spatial extent of these peaks by plotting the peak intensity profile integrated inside a 3.6 eV energy window centered at 528.5 eV. The error bar shown in Fig. 8(d) was

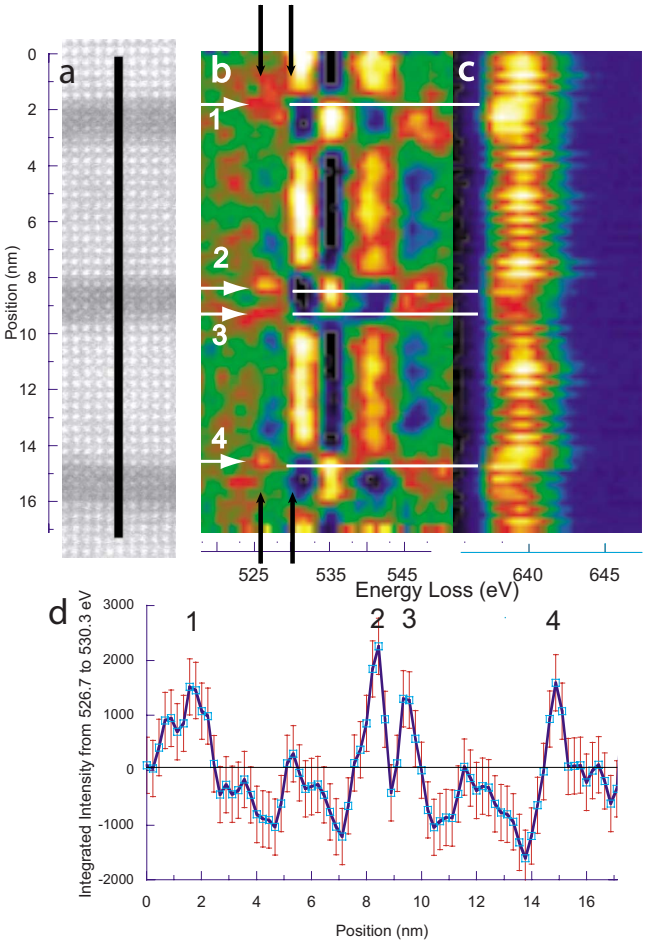

FIG. 8. (Color online) (a) STEM image with EELS line profile drawn. (b) The difference map of the O K edge shows extra spectral weight at the sharp interfaces in the energy range of 526 to 531 eV. The extra spectral weight is confined to an area of 4.5 Å or approximately 1 u.c. The same positions with the extra spectral weight have a (c) abrupt shift in the maximum of the Mn L_3 edge. (d) An integrated intensity profile from 526.7 to 530.3 eV shows the extra O K spectral weight is above the background noise level.

estimated from the background noise before the background subtracted O K edge. The four peaks identified in Figs. 8(b) and 8(d) are clearly above the background noise. By fitting these peaks with a Gaussian peak, we measured the FWHM of the extra interfacial states for position 2 and 4 at 3.9 Å and 5.2 Å, respectively. Therefore, the extent of the interfacial states is spatially confined to approximately one unit cell (3.9 Å).

V. DISCUSSION

In the previous section, we have identified an additional spectral weight at the onset of the O K edge at the sharp interface between the SMO and LMO films in the superlattice. Here we will discuss its significance. The second part of this discussion is on the effect of electron-beam irradiation, which will be ruled out as a cause of our observation. First, we compare the experimental result of our EELS measurement with the RSXS measurement of interfacial states re-

ported by Smadici *et al.*[10] The RSXS measurement was carried out for the intensity of the superlattice reflection with $l=3$ for a $(LMO)_8/(SMO)_4$ superlattice.

Smadici *et al.* observed a peak by tuning the x-ray energy to 530.2 eV near the O *K* edge close to the Fermi level. The peak intensity increases as the temperature decreases. At room temperature, which is the sample temperature for our EELS measurement, the peak is weak but observable in the RSXS measurements. The extra peak intensity at $l=3$ for a $(LMO)_8/(SMO)_4$ superlattice suggests the presence of interfacial states, thus, a very different interfacial bond or interfacial electronic reconstruction. These interfacial states were related to the interfacial magnetization.[7,9,10] The peak intensity measured by RSXS has contributions from all the interfaces in the LMO/SMO superlattice. Since the peak is observed near the O *K* edge, the electronic-structure difference likely is in the Mn-O bond.

The extra spectral weight reported by Smadici *et al.* was also observed by EELS at the onset of the O *K* edge. The measurement was mapped in real space by scanning along the direction normal to the interface. Thus, the difference map plotted in Fig. 8 was obtained by Eq. (1). The advantage of EELS real spacing mapping is that the spatial extent of the interfacial electronic states can be measured directly; this information is not available from RSXS. Second, the EELS measurement can be performed on individual interfaces. The average FWHM from the sharp interfaces of 2 and 4 marked in Fig. 8 is 4.5 Å, about one perovskite unit cell. This number is consistent with theoretical results of Nanda and Satpathy, which predicted that the e_g electron transfer occurs mostly between the two layers adjacent to the interface.[7]

The EELS data show local variations among several supercell interfaces. A large difference is observed between the sharp and rough interfaces, as demonstrated in Figs. 5 and 8, especially the spectral weight attributed to the extra unoccupied states at the onset of the O *K* edge is much larger at the sharp interfaces than the rough interfaces. The difference between the rough interface and sharp interfaces is the interfacial flatness; at the sharp interface the interface is atomically flat while the rough interface consists of interfacial atomic steps over one to two unit-cell width. There are two possible causes for the lack of, or weak, interfacial states at the rough interfaces. One is that the interfacial states are spread over the interface area, which leads to the significantly reduced signals that are difficult to detect by EELS. The other possibility is from the effect of strain and the difference in strain between the sharp and rough interfaces. All superlattices are coherently strained as shown in Sec. III. At the sharp interface, the LMO is under an in-plane compressive strain of 2.1% based on the average *a* and *c* lattice constants while the SMO is under an in-plane tensile strain of 2.5%. Normal to the interface, the LMO and SMO layers experience a tensile and a compressive strain, respectively. The rough interface was the result of noninteger number of unit cells in the LMO layer thickness; the STEM results suggest that this led to a rough growth front of the LMO layer with hills and valleys of 2–3 u.c. in height and the valleys are filled and smoothed out by SMO layers. This growth mechanism resulted in the wavy interfaces between LMO and SMO that were discussed in Sec. III. At the wavy interface, the strain in the normal direction is reduced by the presence of LaO and SrO units in the same layer. Experimentally, it has been demonstrated that substantial change in strain condition can alter the orbital ordering and the dependent interfacial electronic structure.[9,37] Especially, the linear and circular magnetic dichroism study of $(SMO)_n/(LMO)_{2n}$ superlattices by Aruta *et al.*[24] show that charge redistribution across the strained, sharp, interface favors $e_g(x^2\text{-}y^2)$ orbital occupation. The results here suggest that the strain normal to the interface also plays a role in the interfacial orbital ordering.

Mn ions in high oxidation state are susceptible to electron-beam-induced reduction. Riedl and collaborators studied $La_{0.7}Sr_{0.3}MnO_3$ films in which they acquired EELS with increasing dose of electrons.[38] They found that the threshold for damage at 300 kV is 5×10^9 e^-/nm^2 for the O *K* edge and 1×10^{10} e^-/nm^2 for the Mn $L_{2,3}$ edge. With a dose of 1.6×10^{10} e^-/nm^2, the O *K* prepeak nearly disappears and the intensity of third peak is only ~10% greater than the minimum following the second peak. Correspondingly, the ratio of the maximum intensity of the Mn L_2 peak to L_3 peak falls from ~0.6 to ~0.4. The electron dose used in our experiment is 4.5×10^{10} e^-/nm^2 at 80 kV. The lower electron acceleration voltage is used to avoid the electron knock-on damage; the estimated knock-on damage threshold for oxygen is 260 kV based on the displacement energy of 45 eV.[39,40] The other damage mechanism is radiolysis caused by electron-beam-induced charging, which does not have a threshold for high energy electrons.[39] Compared to the results of Riedl *et al.*, the O *K* prepeak in our spectra presented in Fig. 7 is strong and the intensity of the third peak is ~90% and ~40% greater than the minimum following the second peak for LMO and SMO, respectively. Correspondingly, the ratio of the maxima of the L_2 to L_3 peaks in Fig. 6 is ~0.6 for both LMO and SMO. Both show no evidence of electron-beam-induced damage. This is also confirmed by the comparison of the XAS and EELS data as presented for the Mn $L_{2,3}$ edge. Other than the difference in energy resolution, there was no change in the edge fine structure of XAS and EELS. For radiolysis, no evidence of mass loss was found at 80 kV in the HAADF-STEM image. However, in other experiments on similar oxides, we did observe a reduction in the HAADF-STEM image intensity after high spatial resolution EELS line scans at 200 kV after significant beam exposure. Therefore, we rule out electron-beam damage as cause to the observed EELS fine structures in this experiment.

VI. CONCLUSION

In summary, we have presented EELS evidence of interfacial states and mapped their distribution in a LMO/SMO superlattice. The structure of the superlattice is asymmetrical with sharp LMO/SMO and rough SMO/LMO interfaces. The rough SMO/LMO interface is characterized by the mixture of two lattices and steplike contrast in the HAADF-STEM images separated at about 10–20 nm apart. Both the LMO and SMO layers are strained normal to the interface and coherent with the STO substrate lattice in the parallel directions. Spatially resolved EELS spectra were obtained using a

fine aberration corrected electron probe; the resolution is sufficient to allow the mapping of the electronic structure of individual Mn-O atomic columns. Good agreement was obtained between the averaged EELS spectrum and the XAS spectrum obtained from the same sample. Analysis of the EELS spectra at interfaces revealed an additional spectral weight at the onset of the O *K* edge in agreement with the reported RSXS data. The additional spectral weight is distributed at the interface of LMO and SMO with a full-width at half maximum of 1 u.c. The spectral weight is strongest at the sharp interface; it is weak or absent at the rough interfaces.

ACKNOWLEDGMENT

Research in this manuscript was carried out at the Frederick Seitz Materials Research Laboratory Central Facilities, University of Illinois, which are partially supported by the U.S. Department of Energy under Grants No. DE-FG02-07ER46453 and No. DE-FG02-07ER46471, the National Center for Electron Microscopy, Lawrence Berkeley Laboratory, which is supported by the U.S. Department of Energy under Grant No. DE-AC02-05CH11231 and Argonne National Laboratory which is supported by the Office of Basic Energy Sciences, U.S. Department of Energy under Grant No. DE-AC02-06CH11357.

[1] A. Ohtomo, D. A. Muller, J. L. Grazul, and H. Y. Hwang, Nature (London) **419**, 378 (2002).
[2] A. Ohtomo and H. Y. Hwang, Nature (London) **427**, 423 (2004).
[3] S. Okamoto and A. J. Millis, Nature (London) **428**, 630 (2004).
[4] A. Bhattacharya, S. J. May, S. G. E. te Velthuis, M. Warusawithana, X. Zhai, B. Jiang, J.-M. Zuo, M. R. Fitzsimmons, S. D. Bader, and J. N. Eckstein, Phys. Rev. Lett. **100**, 257203 (2008).
[5] C. Adamo, X. Ke, P. Schiffer, A. Soukiassian, M. Warusawithana, L. Maritato, and D. G. Schlom, Appl. Phys. Lett. **92**, 112508 (2008).
[6] S. Dong, R. Yu, S. Yunoki, G. Alvarez, J.-M. Liu, and E. Dagotto, Phys. Rev. B **78**, 201102 (2008).
[7] B. R. K. Nanda and S. Satpathy, Phys. Rev. B **79**, 054428 (2009).
[8] S. Okamoto and A. J. Millis, arXiv:cond-mat/0507150 (unpublished).
[9] C. Aruta, C. Adamo, A. Galdi, P. Orgiani, V. Bisogni, N. B. Brookes, J. C. Cezar, P. Thakur, C. A. Perroni, G. De Filippis, V. Cataudella, D. G. Schlom, L. Maritato, and G. Ghiringhelli, Phys. Rev. B **80**, 140405 (2009).
[10] S. Smadici, P. Abbamonte, A. Bhattacharya, X. Zhai, B. Jiang, A. Rusydi, J. N. Eckstein, S. D. Bader, and J.-M. Zuo, Phys. Rev. Lett. **99**, 196404 (2007).
[11] H. Nakao, J. Nishimura, Y. Murakami, A. Ohtomo, T. Fukumura, M. Kawasaki, T. Koida, Y. Wakabayashi, and H. Sawa, J. Phys. Soc. Jpn. **78**, 024602 (2009).
[12] S. J. May, A. B. Shah, S. G. E. te Velthuis, M. R. Fitzsimmons, J. M. Zuo, X. Zhai, J. N. Eckstein, S. D. Bader, and A. Bhattacharya, Phys. Rev. B **77**, 174409 (2008).
[13] P. D. Nellist, M. F. Chisholm, A. R. Lupini, A. Borisevich, W. H. Sides, Jr., S. J. Pennycook, N. Dellby, R. Keyse, O. L. Krivanek, M. F. Murfitt, and Z. S. Szilagyi, J. Phys.: Conf. Ser. **26**, 7 (2006).
[14] O. L. Krivanek, P. D. Nellist, N. Dellby, M. F. Murfitt, and Z. Szilagyi, Ultramicroscopy **96**, 229 (2003).
[15] H. Müller, S. Uhlemann, P. Hartel, and M. Haider, Microsc. Microanal. **12**, 442 (2006).
[16] S. J. Pennycook, B. Rafferty, and P. D. Nellist, Microsc. Microanal. **6**, 343 (2000).
[17] A. Bhattacharya, X. Zhai, M. Warusawithana, J. N. Eckstein, and S. D. Bader, Appl. Phys. Lett. **90**, 222503 (2007).
[18] C. Kisielowski *et al.*, Microsc. Microanal. **14**, 469 (2008).
[19] Y. Zhu, R. Klie, T. Tomita, H. Sawada, and K. Nagahata, Microsc. Microanal. **11**, 1428 (2005).
[20] J. G. Wen, J. Mabon, C. Lei, S. Burdin, E. Sammann, I. Petrov, A. B. Shah, V. Chobpattana, J. Zhang, K. Ran, J.-M. Zuo, S. Mishina, and T. Aoki, Microsc. Microanal. **16**, 183 (2010).
[21] J. Rodríguez-Carvajal, M. Hennion, F. Moussa, A. H. Moudden, L. Pinsard, and A. Revcolevschi, Phys. Rev. B **57**, R3189 (1998).
[22] T. Negas and R. S. Roth, J. Solid State Chem. **1**, 409 (1970).
[23] M. Gao, J. M. Zuo, R. D. Twesten, I. Petrov, L. A. Nagahara, and R. Zhang, Appl. Phys. Lett. **82**, 2703 (2003).
[24] C. Aruta, G. Ghiringhelli, V. Bisogni, L. Braicovich, N. B. Brookes, A. Tebano, and G. Balestrino, Phys. Rev. B **80**, 014431 (2009).
[25] H. Kurata and C. Colliex, Phys. Rev. B **48**, 2102 (1993).
[26] J. H. Rask, B. A. Miner, and P. R. Buseck, Ultramicroscopy **21**, 321 (1987).
[27] Z. L. Wang, J. S. Yin, and Y. D. Jiang, Micron **31**, 571 (2000).
[28] J. Verbeeck, O. I. Lebedev, G. Van Tendeloo, J. Silcox, B. Mercey, M. Hervieu, and A. M. Haghiri-Gosnet, Appl. Phys. Lett. **79**, 2037 (2001).
[29] A. B. Shah, X. Zhai, B. Jiang, J.-G. Wen, J. N. Eckstein, and J.-M. Zuo, Phys. Rev. B **77**, 115103 (2008).
[30] J. Verbeeck, O. I. Lebedev, G. Van Tendeloo, and B. Mercey, Phys. Rev. B **66**, 184426 (2002).
[31] M. Abbate, F. M. F. de Groot, J. C. Fuggle, A. Fujimori, O. Strebel, F. Lopez, M. Domke, G. Kaindl, G. A. Sawatzky, M. Takano, Y. Takeda, H. Eisaki, and S. Uchida, Phys. Rev. B **46**, 4511 (1992).
[32] W. D. Luo, M. Varela, J. Tao, S. J. Pennycook, and S. T. Pantelides, Phys. Rev. B **79**, 052405 (2009).
[33] M. Varela, M. P. Oxley, W. Luo, J. Tao, M. Watanabe, A. R. Lupini, S. T. Pantelides, and S. J. Pennycook, Phys. Rev. B **79**, 085117 (2009).
[34] J. Gazquez, M. Varela, M. P. Oxley, M. Torija, M. Sharma, C. Leighton, and S. J. Pennycook, Microsc. Microanal. **14**, 1354 (2008).
[35] G. Yang, Y. Zhao, K. Sader, A. Bleloch, and R. F. Klie, Microsc. Microanal. **14**, 436 (2008).
[36] J. H. Paterson and O. L. Krivanek, Ultramicroscopy **32**, 319 (1990).

[37] H. Yamada, M. Kawasaki, T. Lottermoser, T. Arima, and Y. Tokura, Appl. Phys. Lett. **89**, 052506 (2006).
[38] T. Riedl, T. Gemming, and K. Wetzig, International Workshop on Enhanced Data Generated by Electrons (EDGE 2005), Grundlsee, Austria, 2005 (unpublished).
[39] R. F. Egerton, P. Li, and M. Malac, Micron **35**, 399 (2004).
[40] K. L. Smith, R. Cooper, M. Colella, and E. R. Vance, *Scientific Basis for Nuclear Waste Management XXIV*, MRS Symposia Proceedings No. 663 (Materials Research Society, Pittsburgh, 2001), p. 373.